THE JOURNAL OF PHYSICAL CHEMISTRY C
A JOURNAL OF THE AMERICAN CHEMICAL SOCIETY

pubs.acs.org/JPCC

Article

Photothermally Probing Vibrational Excited-State Absorption with Nanoscale Spatial Resolution through Frequency-Domain Pump–Probe Peak Force Infrared Microscopy

Haomin Wang, Qing Xie, Yu Zhang, and Xiaoji G. Xu*

Cite This: J. Phys. Chem. C 2021, 125, 8333–8338

Read Online

ACCESS | Metrics & More | Article Recommendations | Supporting Information

ABSTRACT: The diffraction limit binds the spatial resolution of optical spectroscopy to a finite fraction of the light wavelength. Traditional far-field pump/probe spectroscopy that detects the excited-state absorption (ESA) is not an exception. In this work, we present a new spectroscopic route to measure ESA based on the mechanical detection of the photothermal responses with the peak force infrared (PFIR) microscopy. We probe the vibrational ESA through the difference of the photothermal effects between temporal overlap and offset of two frequency-tunable infrared pulses. Two-dimensional PFIR spectra are collected on the carbonyl of a polymer with ESA responses. Also, we spatially map the ESA response of a structured polymer. The spatial resolution of the pump–probe PFIR microscopy is not bound by the diffraction limit that restraints to a finite fraction of the wavelength. Further, implementation of the detection paradigm of pump–probe microscopy will provide access to the highly desired two-dimensional infrared nanoscopy.

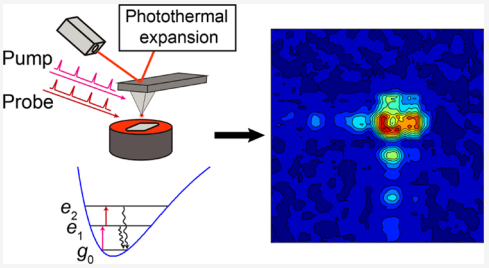

INTRODUCTION

Vibrational excited-state absorption (ESA) is the absorption of a photon from a lower excited vibrational level to a higher excited vibrational level of a molecule. ESA typically occurs in sequential photon absorptions: the first photon excites the molecule from the ground state to the first excited state, followed by the second photon that connects the first excited state to the second excited state. Because of the anharmonicity of the vibrational levels, the photon energy associated with ESA is less than the fundamental vibrational transition. Therefore, the spectroscopy of vibrational ESA can probe the anharmonicity of potential energy surfaces, investigate the interaction between the vibrational modes, deduce molecular structures, and reveal excited-state dynamics.[1−6]

ESA of vibrational levels is usually studied by infrared pump/probe spectroscopy or two-dimensional infrared spectroscopy. However, the spatial resolution of the measurement is bound by Abbe's diffraction limit. The photons involved in the ESA measurement cannot be focused to a spot smaller than a half of their wavelength, that is, several microns in the mid-infrared. Although there exists configurations of far-field pump/probe microscopies in the visible/near-infrared that achieves the sub-diffraction limit by a factor of two through spatial tailoring or modulation of the optical field, their resolutions are still linked to the wavelength of the light.[7−9] Atomic force microscopy (AFM)-based pump–probe microscopy has been developed through near-field detection[10−12] or the detection of photo-induced dipole–dipole force.[13] However, they have not been applied to study molecular excited vibrational levels in the mid-infrared.

In this study, we seek to bypass the diffraction limit in probing vibrational ESA with a new detection paradigm—through detection of the difference of the photothermal effect. We incorporate the frequency-domain pump–probe technique with the peak force infrared (PFIR) microscopy[14] to identify the additional photothermal effect generated by the photon absorption of the probe pulse in ESA. The infrared-induced photothermal expansion is mechanically detected with a sharp AFM tip. Consequently, the spatial resolution of this method is well below the optical diffraction limit and not linked to the wavelength of the light.

While the conventional pump–probe spectroscopy and microscopy focus either on the attenuation or gain of the probe pulse with the presence of the pump pulse, our approach measures the modification of the photothermal effect of the probe absorption due to the presence of the pump. Without the presence of the pump pulse, the ESA transition by the probe will not occur even if the probe frequency is tuned to match the transition between the first vibrational state e_1 and the second vibrational state e_2. The lifetimes of the vibrational excited states are in the order of picoseconds. If the separation between the pump and probe pulses are much larger than the vibrational lifetime, that is, on the nanosecond scale, the

Received: February 10, 2021
Revised: March 21, 2021
Published: April 8, 2021

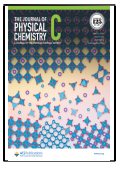

https://doi.org/10.1021/acs.jpcc.1c01268
J. Phys. Chem. C 2021, 125, 8333–8338

modification of the absorption of the probe by the pump is negligible. Therefore, the intensity modulation of the pump pulse in the conventional optical pump−probe spectroscopy can be substituted by a temporal modulation of the timing of the pump pulse to cause a difference in the photothermal signal. In our case, we use two narrowband frequency-tunable infrared lasers with nanosecond-level durations. At a large temporal displacement of tens of nanoseconds, the individual infrared absorptions of the pump and probe pulses are considered as non-interacting events, and no ESA will occur.

To understand the operational mechanism of the frequency-domain pump−probe PFIR microscopy to access ESA, let us first examine the heat generation pathways with narrowband laser pulses. The potential energy surface (PES) of the electronic ground state supports a series of vibrational levels. The three low vibrational states are g_0, e_1, and e_2. The frequency of the pump pulse ω_{pu} is tuned to match the first vibrational transition with $\hbar\omega_{pu} = E(e_1) - E(g_0)$; the frequency of the probe pulse ω_{pr} is tuned to match the overtone with $\hbar\omega_{pr} = E(e_2) - E(e_1)$. When the pump pulse illuminates the molecule, the transition between g_0 and e_1 happens, causing a fraction of the population to transit into e_1. For the convenience of bookkeeping, the probability of this first transition is defined as α. When the probe illuminates together with the pump, a subset of the population at e_1 prepared by the pump is excited to e_2 by the probe. The probability of the second transition is defined as β. After vibrational relaxation lifetime, the populations at e_1 and at e_2 find ways to relax to the ground state g_0, thereby releasing heat and increasing the temperature in the process, as described in Figure 1a.

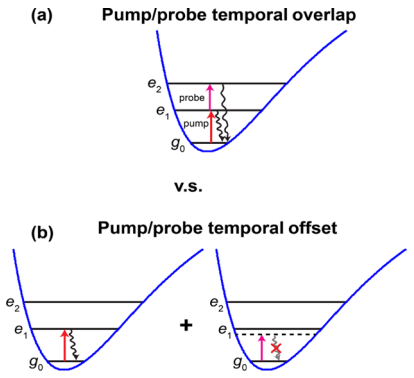

Figure 1. Heat generation pathways in pump−probe PFIR. (a) When the pump and probe overlap, the heat generation increases due to the additional thermal relaxation caused by the $e_1 \rightarrow e_2$ absorption. (b) When the pump and probe do not overlap, the heat generation is only resulted from the $g_0 \rightarrow e_1$ absorption. Note that due to the anharmonicity of PES, the energy difference between states e_1 and g_0 is greater than the energy difference between the states e_2 and e_1.

The amount of heat generated from the relaxation of e_1 is denoted as $Q_1 = N\hbar\omega_{pu}\alpha(1-\beta)$; and the heat generated from the relaxation of e_2 is $Q_2 = N\hbar(\omega_{pu} + \omega_{pr})\alpha\beta$. N is the average number of molecules within the excitation volume. The combined heat from both states is $Q = Q_1 + Q_2 = N\hbar(\omega_{pu}\alpha + \omega_{pr}\alpha\beta)$. If the pump and probe pulses have enough temporal offset outside the vibrational relaxation time, the pump pulse is still capable of promoting the transition between g_0 and e_1. However, the probe pulse cannot access the transition between e_1 and e_2, because the population at e_1 has already relaxed to g_0, as Figure 1b describes. The heat generation, in this case, is only from the relaxation of the population from e_1, which is $Q' = N\hbar\omega_{pu}\alpha$. The heat difference between the conditions of pump−probe overlap and temporal offset is then $\Delta Q = Q - Q' = N\hbar\omega_{pr}\alpha\beta$, which is equal to the total absorbed photon energy in the transition between e_1 and e_2, which is ESA. Therefore, ESA can be measured by detecting the heat difference of the pump−probe being overlapped or offset. In the AFM-based photothermal microscopy, the heat generation leads to the photothermal effect, which is translated into the mechanical signal of the AFM cantilever. The AFM detection of the infrared photothermal expansion has been widely used as a signal generation mechanism in linear AFM-IR microscopies, such as photothermal-induced resonance, photo-induced force microscopy, and the regular PFIR microscopy.[14−17]

METHODS

Figure 2a schematically illustrates the experimental construction of frequency-domain pump−probe PFIR microscopy with two narrowband infrared light sources. Two separate quantum cascade lasers (QCL, MIRcat, and MIRcat-QT from Daylight Solutions) are used to provide frequency-tunable infrared radiations of 20 to 1000 ns duration. One of the outputs of the two QCLs is designated as the "pump", and the other is the "probe". The output of the laser pulses from the two QCLs are combined with a 50:50 infrared beam splitter and are guided onto the tip-sample region with reflective optics. The combined laser beams are focused by a parabolic mirror of 25 mm effective focal length to reach the gold-coated AFM tip (RTESP-150, Bruker). The AFM tip acts as an optical antenna and enhances the infrared field underneath, leading to enhanced infrared absorptions and photothermal expansions.

A digital delay generator (DDG, DG645 Stanford Research Systems) is used to trigger the QCLs to generate laser pulses with adjustable time delays on-demand. The photothermal detections of the infrared absorption is done with a custom-built PFIR microscope, described in the literature.[14] An atomic force microscope (Multimode 8, Bruker) is operated in the peak force tapping (PFT) mode. The AFM tip intermittently touches the sample surface at the PFT frequency of 4 kHz. The PFT frequency is routed to a lock-in amplifier (MFLi, Zurich Instruments), acting as a phase-locked loop to generate a transistor-to-transistor logical (TTL) waveform at the exact PFT frequency. One replica of the TTL waveform is routed to the MIRcat QCL as an external trigger to generate a series of infrared pulses as the probe. Then, the TTL waveform is reduced to 1 kHz by a circuit of D-flip-flop and is routed to the DDG as a trigger. Therefore, the DDG is triggered after every four PFT cycles. At each trigger, the DDG generates a waveform of four TTL triggers with slight temporal offsets from the original TTL at PFT frequency (Figure 2b). This customized TTL waveform from DDG is routed to the MIRcat-QT QCL as an external trigger to generate infrared pulses as the pump. Consequently, for every four pump−probe pulse pairs emitted from the QCLs, the first pulse pair temporally overlaps. The second, third, and fourth pulse pairs are temporally offset, for example, by 20, 25, and 30 ns, respectively. The pump−probe pulse pair with temporal overlap is capable of exciting ESA; the rest of the three pulse pairs are utilized as the background photothermal effects without ESA.

https://doi.org/10.1021/acs.jpcc.1c01268
J. Phys. Chem. C 2021, 125, 8333−8338

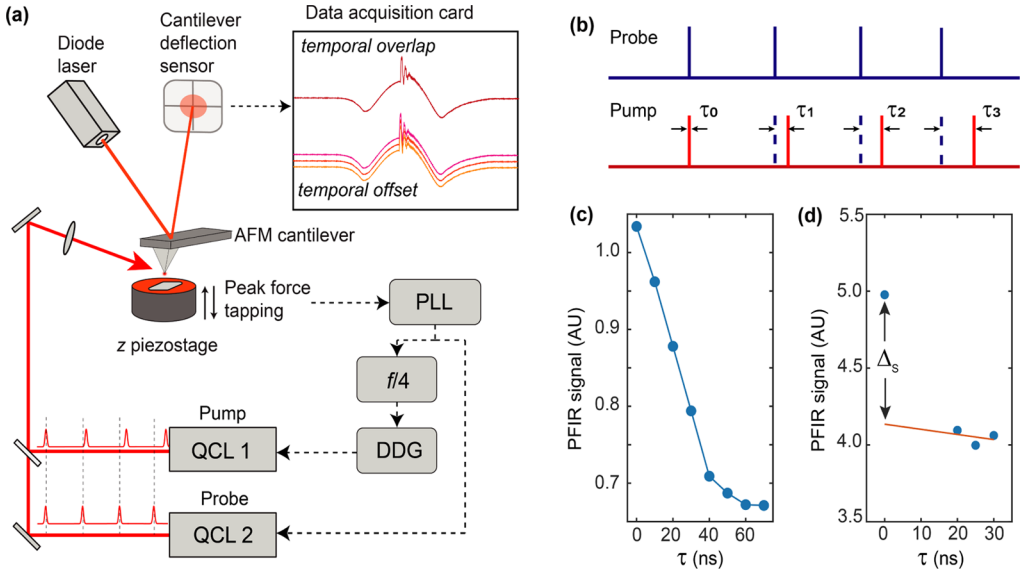

Figure 2. Experimental setup and the mechanism of pump−probe PFIR microscopy. (a) Experimental setup of the pump−probe PFIR microscopy. An AFM and two QCL laser sources are included. The cantilever deflection from the quadrant detector is monitored and recorded by a DAQ card. (b) Time delays between the probe and pump in every four PFT cycles. The first pump−probe pair is overlapped ($\tau_0 = 0$), and the rest of the three delays are increasing ($\tau_1 < \tau_2 < \tau_3$). (c) PFIR signal S versus the time delay τ measured on the PMMA-N3 sample when both pump and probe frequencies are non-absorbing ($\omega_{pump} = \omega_{probe} = 1600\ cm^{-1}$). The signal drops linearly between 0 and 40 ns. (d) Illustration of the signal processing procedure of the pump−probe PFIR. Four experimentally collected ($\omega_{pump} = 1711\ cm^{-1}$ and $\omega_{probe} = 1728\ cm^{-1}$) PFIR signals are plotted against τ_0 (0), τ_1 (20 ns), τ_2 (25 ns), and τ_3 (30 ns). The last three signals are extrapolated toward $\tau = 0$, and the difference between the signal measured at τ_0 and the extrapolated signal, designated as ΔS, is used as the pump−probe PFIR signal.

The infrared absorption in the sample generates the photothermal expansions, which are mechanically detected by the dynamic deflection of the AFM cantilever. A quadrant photodiode is used to register the vertical deflection of the AFM cantilever, and the voltage from the quadrant photodiode is digitalized by a data acquisition (DAQ) card (PXI-5122, National Instruments). The infrared photothermal expansion of the sample mechanically vibrates the AFM cantilever through the dynamic contact between the tip and the sample. Transient cantilever oscillations are acquired by the DAQ card and then Fourier-transformed into the oscillation amplitude as the PFIR signal. The differences in the photothermal signals between the pump−probe in the overlap and offsets are processed to obtain the pump−probe PFIR signals.

One challenge in detecting the difference in the photothermal effects is the thermal relaxation of the sample affecting the mechanical detection by the AFM cantilever deflection. In AFM-IR or PFIR microscopy with single-pulse excitation, the mechanical response of the AFM cantilever is treated to be proportional to the amount of heat generated by the infrared absorption from the laser pulse. However, if there are two optical pulses with temporal separation comparable to the heat relaxation time, the photothermal mechanical perturbation to the AFM cantilever will be affected by the temporal separation. Figure 2c displays an experimentally collected PFIR signal as a function of the temporal offset between two off-resonant infrared pump−probe pulses of 20/80 ns duration. A rapid decreasing trend is observed. At off-resonant infrared frequencies, the photothermal signal is not enhanced by a particular spectroscopic absorption, and no sequential light absorption effect such as ESA will occur. In Figure 2c, only the timing of the pulses is changed. The total intensities of the two pulses remain the same during the time scan. However, the photothermal expansion signal detected by the AFM cantilever rapidly decreases as the temporal separation between the two pulses is increased.

Such a signal decrease is due to the thermal diffusion of the sample. After the sample is excited by a nanosecond pump pulse, the temperature of the sample suddenly rises and then decreases over time due to heat diffusion.[18−20] If the second laser pulse arrives shortly after the first, the second photothermal effect is generated in addition to that of the first one. The maximal photothermal expansion by the two pulses with temporal offset is smaller than the direct sum of the two individually arriving pulses,[21] which is equivalent to the condition of temporal overlap but hypothetically without joint spectroscopic processes. On the other hand, the maximal cantilever deflection is determined by the maximal amplitude of the photothermal expansion within the mechanical response time of the AFM cantilever. Thus, the measured photothermal expansion when the pump and probe pulses are temporally offset is smaller than the condition when they temporally overlap but hypothetically without joint spectroscopic pathways. In other words, the true photothermal signal background is the photothermal expansion when the pump and probe pulses temporally overlap, but the joint spectroscopic pathways are absent.

To eliminate such a hypothetical background from the detection of the difference of the photothermal effect due to joint spectroscopic pathways, we use an empirical treatment to compensate for the heat diffusion. We perform a linear fit of the PFIR signals S to the temporal offset τ between the pump and probe pulses. Then, a linear trend from the three temporal offset conditions (e.g., 20, 25, and 30 ns) is extrapolated back to $\tau = 0$ ns to obtain the would-be photothermal background, where no additional joint spectroscopic pathways, including ESA, were present. The procedure of the extrapolation is illustrated in Figure 2d. The difference between the

https://doi.org/10.1021/acs.jpcc.1c01268
J. Phys. Chem. C 2021, 125, 8333−8338

experimentally measured signal S at τ_0 and the extrapolation at $\tau = 0$ is designated as ΔS and used as the pump−probe PFIR signal to represent the photothermal signal due to the combined light−matter interactions from both pump and the probe pulses. The frequencies of the pump and probe pulses are scanned in two dimensions to register the pump−probe PFIR signals to form a two-dimensional PFIR spectrum.

RESULTS

We tested the frequency-domain pump−probe PFIR spectroscopy on ω-azide-terminated PMMA (PMMA-N3) polymer films. The FTIR spectra of the PMMA-N3 is provided in Figure S1. PMMA-N3 is a suitable sample for demonstration because it has a sharp IR absorption peak at 1728 cm^{-1} and no other absorptions within the 1650−1800 cm^{-1} region.[22]

Figure 3a shows the normalized frequency-domain pump−probe PFIR spectrum of the PMMA-N3 illustrated by a contour map, with the intensity of ΔS being represented by the false color. Besides a strong photothermal effect around 1728/1728 cm^{-1}, four distinct photothermal ESA responses at pump/probe frequencies of 1690/1728, 1728/1690, 1710/1728, and 1728/1710 cm^{-1} (pointed by white arrows) become visible, and they are symmetrical along the diagonal. The photothermal responses of 1710 and 1690 cm^{-1} correspond to the excited-states' absorption between states e_1 to e_2 and e_2 to e_3, respectively. ESA absorption that corresponds to e_2 to e_3 is due to the vibrational resonance having a finite linewidth. Therefore, excitation with infrared frequency of 1728 cm^{-1} is still capable of promoting transitions from e_1 to e_2 to serve as an intermediate step prior to the transition between e_2 and e_3 by infrared frequency 1690 cm^{-1}, albeit at low efficiency. Photothermal ESA responses are symmetrical along the diagonal in the two-dimensional spectrum because the pump−probe PFIR measures the overall heat effect, and the pump and probe are interchangeable. Our pump−probe PFIR method reveals two ESA absorptions of the PMMA-N3 at 1710 and 1690 cm^{-1}, which are due to anharmonicities of the C═O vibrations.

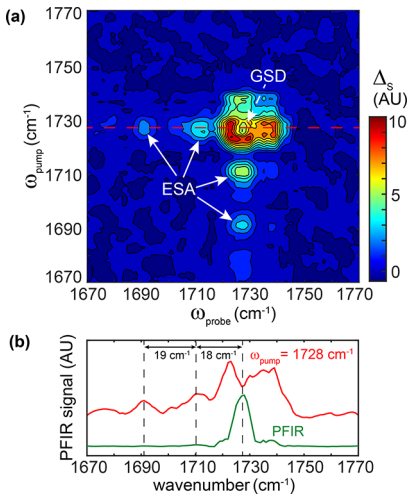

Figure 3. Two-color PFIR spectrum of PMMA-N3 and sectional profile. (a) Two-color PFIR spectrum. White arrows indicate the locations of ESA, and a dashed white arrow is pointing at the location of GSD. The pump−probe pulse durations are 20 and 80 ns, respectively. The four time delays are $\tau_0 = 0$, $\tau_1 = 20$ ns, $\tau_2 = 25$ ns, and $\tau_3 = 30$ ns (see Figure 2b). The regular ground-state PFIR spectrum (green, without pump beam) and a sectional profile of the pump−probe PFIR spectrum (red) are shown in (b). The sectional profile is extracted at $\omega_{pump} = 1728$ cm^{-1} along the red dashed line in (a).

The sectional profile of the two-dimensional spectrum at $\omega_{pump} = 1728$ cm^{-1} is displayed (red curve) in Figure 3b. A dip is observed at 1728/1728 cm^{-1} (indicated by the dashed arrow), which can be attributed to the ground-state depletion (GSD). The regular PFIR spectrum of the same sample is included as a reference (green curve), which confirms the strong C═O vibrational absorption at 1728 cm^{-1}. ESA peaks at 1690 and 1710 cm^{-1}, and GSD dip at 1728 cm^{-1} (marked by vertical dashed lines) are observed in the sectional profile (red curve).

Depending on the experimental conditions (e.g., sample and laser frequencies), the photothermal backgrounds decay differently within the time window of nanoseconds. Therefore, the linear fitting procedure shown in Figure 2c may become too risky. To estimate the robustness of our background removal procedure, R-square values from the linear fitting are plotted in Figure S2. The distribution of R-square values along the two pump/probe axes is fairly random, indicating that the interpretation of ESA and GSD phenomena is unlikely caused by systematic error. There are 20% of bad-conditioned linear-fitted pixels with R-square values less than 0.1, which is caused by random noises in the measurement that cannot be overcome by the fitting of limited number of data points. Further improvements can be done by populating the time window with more data points by using the DDG with more outputs. Additionally, if the laser pulse duration is much shorter than the heat diffusion rate, for example, in picoseconds, the photothermal background subtraction procedures would be bypassed, which will reduce the noise in the signal readout.

Nano-imaging using the pump−probe PFIR microscopy is achievable by keeping the pump−probe frequencies at ESA while scanning the AFM tip over the sample surface. In this case, only the surface component that can absorb at ESA frequencies can generate detectable signals of ΔS. Figure 4a

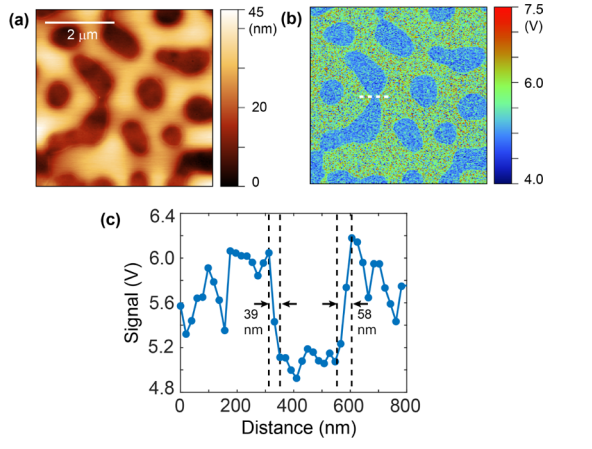

Figure 4. Pump−probe PFIR imaging of phase-separated domains of PS:PMMA-N3. (a) Topography of the PS:PMMA-N3 blend films. The higher domains are PMMA-N3, while the lower domains are PS. (b) Pump−probe PFIR image at $\omega_{pump} = 1726$ cm^{-1} and $\omega_{probe} = 1711$ cm^{-1}; (c) signal profile obtained from the white dashed line in (b). A spatial resolution of ∼40 nm is obtained from the edge of the signal profile.

https://doi.org/10.1021/acs.jpcc.1c01268
J. Phys. Chem. C 2021, 125, 8333−8338

shows the AFM topography of polystyrene (PS):PMMA-N3 blend polymer films, where PS and PMMA-N3 domains are separated due to the spontaneous phase separation. Figure 4b shows pump−probe PFIR images at one pair of ESA frequency of PMMA-N3 with ω_{pump} = 1726 cm^{-1} and ω_{probe} = 1711 cm^{-1}. In the ESA image, PMMA-N3 domains show higher signal intensities of ΔS over PS domains. The ESA image with 1710−1728 cm^{-1} pump−probe frequencies is shown in Figure S3 and is identical to Figure 4b. The PFIR image of the difference between τ_0 and τ_3 at non-ESA frequencies of the same sample is shown in Figure S4, where no contrast can be found, indicating that the ESA imaging is chemically sensitive. To estimate the spatial resolution, a cross-sectioned signal profile from the white dashed line in Figure 4b is plotted in Figure 4c. From the distances within the signal edges, we estimate the spatial resolution of the pump−probe PFIR to be ∼40 nm with our current experimental implementation.

The ESA imaging quality of Figure 4b is inferior to the regular single-frequency PFIR image through linear absorptions (Figure S5). This is because ESA is a much weaker phenomenon, which is usually smaller than 1% of the linear absorption.[23,24] We estimated a small signal-to-noise (S/N) ratio of 1.3 on the PMMA-N3 domains in Figure 4b. From a regular single-frequency PFIR image of a similar area, the S/N ratio is estimated to be 33 (see Figure S5), which is 25 times higher than the ESA imaging. With a lower S/N ratio, ESA imaging is informative in dissecting the distribution of nonlinear absorptions across the sample surface at the nanoscale, which can aid to differentiate the heterogeneous samples if their linear absorptions are overlapped.

DISCUSSION AND CONCLUSIONS

In the photothermal detection mechanism of the frequency-domain pump−probe PFIR microscopy, the role of the pump and probe pulses are interchangeable. Therefore, the experimental 2D pump−probe PFIR spectrum in Figure 3 exhibits a diagonally symmetrical pattern. Also, the terminology of "pump−probe" is different from the popular time-resolved pump−probe spectroscopy, where the temporal domain information reveals the spectroscopic information. Here, the pump and probe simply mean that two separate pulses are used, and one pulse precedes the other. The spectroscopic information is contained in the pump−probe PFIR spectrum through scanning the wavelengths of the two narrowband infrared sources. The background removal procedure that involves scanning the relative temporal offset between the pump and probe pulses in the nanosecond scale (Figure 2c,d) does not contain the temporal information of the molecular vibrational relaxation because the molecular vibrational relaxation is on the much shorter picosecond time scale.

In the pump−probe scattering-type scanning near-field optical microscopy (s-SNOM),[10,11] modifications of the polarizability of the tip-sample junction are measured. The small fraction of the excited-state population leads to only a slight modification of the effective polarizability of the tip-sample junction, which often exhibits very weak ESA signals. In contrast, our pump−probe PFIR microscopy measures the energy dissipation after infrared absorption, which is directly related to the photon absorption, like regular infrared spectroscopy. Therefore, ESA absorption by the carbonyl group of PMMA-N3 is revealed and used as the imaging contrast to map out the structured polymer blends with nanoscale resolution with the frequency-domain pump−probe PFIR. A further application of the frequency-domain pump−probe PFIR microscopy is to study the coupling between molecular vibrational levels and the nanoscale mid-infrared antenna, leading to shifts in the ESA.[6] The small sizes of the mid-infrared antenna are below the diffraction limit, and the spatial resolution of our method can bypass the diffraction limit for *in situ* spectra collection.-

The application of the frequency-domain pump−probe PFIR microscopy can extend beyond the measurement of the vibrational ESA. If the signal-to-noise ratio of the measurement can be further improved beyond the current level, the same measurement principle should be applicable to measure the mode coupling between different vibrational modes with nanoscale spatial resolution—a route toward the 2D-IR nanoscopy. Further development of the pump/probe PFIR microscopy may benefit from the utilization of short-duration femtosecond/picosecond laser sources. The AFM mechanical detection on the difference of photothermal expansions with femtosecond duration pulses will provide access to time-resolved pump/probe nanoscopy. If the pulse duration is shorter than the relaxation time of the excited states, scanning the temporal offset between the pump and the probe within the depopulation time will provide the much-needed temporal resolution toward the spatial−temporal imaging. At the same time, the narrow bandwidth of the picosecond laser is still sufficient for spectral resolution in the collection of the two-dimensional PFIR spectrum.

ASSOCIATED CONTENT

Supporting Information

The Supporting Information is available free of charge at https://pubs.acs.org/doi/10.1021/acs.jpcc.1c01268.

Measurement parameters and preparation of materials, FTIR spectrum of PMMA-N3, *R*-square values of the linear fitting, pump−probe PFIR image at ω_{pump} = 1710 cm^{-1} and ω_{probe} = 1728 cm^{-1}, pump−probe PFIR imaging at non-ESA frequencies, and estimation and comparison of signal-to-noise ratios (PDF)

AUTHOR INFORMATION

Corresponding Author

Xiaoji G. Xu − *Department of Chemistry, Lehigh University, Bethlehem, Pennsylvania 18015, United States;* orcid.org/0000-0003-0847-5871; Email: xgx214@lehigh.edu

Authors

Haomin Wang − *Department of Chemistry, Lehigh University, Bethlehem, Pennsylvania 18015, United States*

Qing Xie − *Department of Chemistry, Lehigh University, Bethlehem, Pennsylvania 18015, United States*

Yu Zhang − *Q-Chem Inc., Pleasanton, California 94588, United States*

Complete contact information is available at: https://pubs.acs.org/10.1021/acs.jpcc.1c01268

Author Contributions

X.G.X conceived the idea and guided overall research. H.W. and Q.X. conducted the experiment. H.W., Y. Z., and X.G.X. contributed to the data interpretation. H.W. and X.G.X. wrote the manuscript.

Notes

The authors declare no competing financial interest.

https://doi.org/10.1021/acs.jpcc.1c01268
J. Phys. Chem. C 2021, 125, 8333−8338

■ ACKNOWLEDGMENTS

X.G.X. would like to thank the support of Sloan Research Fellowship from the Alfred P. Sloan Foundation.

■ REFERENCES

(1) Hamm, P.; Zanni, M. *Concepts and methods of 2D infrared spectroscopy*; Cambridge University Press: Cambridge, U.K., 2011.
(2) Schoonover, J. R.; Strouse, G. F. Time-Resolved Vibrational Spectroscopy of Electronically Excited Inorganic Complexes in Solution. *Chem. Rev.* **1998**, *98*, 1335−1356.
(3) Kraack, J. P. Ultrafast Structural Molecular Dynamics Investigated with 2D Infrared Spectroscopy Methods. *Multidimensional Time-Resolved Spectroscopy*; Springer, 2019; pp 113−205.
(4) Buckup, T.; Léonard, J. Multidimensional Vibrational Coherence Spectroscopy. *Multidimensional Time-Resolved Spectroscopy*; Springer, 2019; pp 207−245.
(5) Baiz, C. R.; Błasiak, B.; Bredenbeck, J.; Cho, M.; Choi, J.-H.; Corcelli, S. A.; Dijkstra, A. G.; Feng, C.-J.; Garrett-Roe, S.; Ge, N.-H.; et al. Vibrational Spectroscopic Map, Vibrational Spectroscopy, and Intermolecular Interaction. *Chem. Rev.* **2020**, *120*, 7152−7218.
(6) Selig, O.; Siffels, R.; Rezus, Y. L. A. Ultrasensitive Ultrafast Vibrational Spectroscopy Employing the Near Field of Gold Nanoantennas. *Phys. Rev. Lett.* **2015**, *114*, 233004.
(7) Massaro, E. S.; Hill, A. H.; Grumstrup, E. M. Super-Resolution Structured Pump-Probe Microscopy. *ACS Photonics* **2016**, *3*, 501−506.
(8) Zhu, Y.; Cheng, J.-X. Transient Absorption Microscopy: Technological Innovations and Applications in Materials Science and Life Science. *J. Chem. Phys.* **2020**, *152*, 020901.
(9) Wang, P.; Slipchenko, M. N.; Mitchell, J.; Yang, C.; Potma, E. O.; Xu, X.; Cheng, J.-X. Far-Field Imaging of Non-Fluorescent Species with Subdiffraction Resolution. *Nat. Photonics* **2013**, *7*, 449−453.
(10) Wagner, M.; Fei, Z.; McLeod, A. S.; Rodin, A. S.; Bao, W.; Iwinski, E. G.; Zhao, Z.; Goldflam, M.; Liu, M.; Dominguez, G.; et al. Ultrafast and Nanoscale Plasmonic Phenomena in Exfoliated Graphene Revealed by Infrared Pump-Probe Nanoscopy. *Nano Lett.* **2014**, *14*, 894−900.
(11) Wagner, M.; McLeod, A. S.; Maddox, S. J.; Fei, Z.; Liu, M.; Averitt, R. D.; Fogler, M. M.; Bank, S. R.; Keilmann, F.; Basov, D. N. Ultrafast Dynamics of Surface Plasmons in InAs by Time-Resolved Infrared Nanospectroscopy. *Nano Lett.* **2014**, *14*, 4529−4534.
(12) Gilburd, L.; Xu, X. G.; Bando, Y.; Golberg, D.; Walker, G. C. Near-Field Infrared Pump-Probe Imaging of Surface Phonon Coupling in Boron Nitride Nanotubes. *J. Phys. Chem. Lett.* **2016**, *7*, 289−294.
(13) Jahng, J.; Brocious, J.; Fishman, D. A.; Yampolsky, S.; Nowak, D.; Huang, F.; Apkarian, V. A.; Wickramasinghe, H. K.; Potma, E. O. Ultrafast Pump-Probe Force Microscopy with Nanoscale Resolution. *Appl. Phys. Lett.* **2015**, *106*, 083113.
(14) Wang, L.; Wang, H.; Wagner, M.; Yan, Y.; Jakob, D. S.; Xu, X. G. Nanoscale Simultaneous Chemical and Mechanical Imaging via Peak Force Infrared Microscopy. *Sci. Adv.* **2017**, *3*, No. e1700255.
(15) Nowak, D.; Morrison, W.; Wickramasinghe, H. K.; Jahng, J.; Potma, E.; Wan, L.; Ruiz, R.; Albrecht, T. R.; Schmidt, K.; Frommer, J.; et al. Nanoscale Chemical Imaging by Photoinduced Force Microscopy. *Sci. Adv.* **2016**, *2*, No. e1501571.
(16) Dazzi, A.; Glotin, F.; Carminati, R. Theory of Infrared Nanospectroscopy by Photothermal Induced Resonance. *J. Appl. Phys.* **2010**, *107*, 124519.
(17) Jahng, J.; Potma, E. O.; Lee, E. S. Tip-Enhanced Thermal Expansion Force for Nanoscale Chemical Imaging and Spectroscopy in Photoinduced Force Microscopy. *Anal. Chem.* **2018**, *90*, 11054−11061.
(18) Volz, S. *Thermal Nanosystems and Nanomaterials*; Springer, 2009; Vol. *118*.
(19) Chen, X.; Chen, Y.; Yan, M.; Qiu, M. Nanosecond Photothermal Effects in Plasmonic Nanostructures. *ACS Nano* **2012**, *6*, 2550−2557.
(20) Hu, M.; Hartland, G. V. Heat Dissipation for Au Particles in Aqueous Solution: Relaxation Time versus Size. *J. Phys. Chem. B* **2002**, *106*, 7029−7033.
(21) Quaroni, L. Understanding and Controlling Spatial Resolution, Sensitivity, and Surface Selectivity in Resonant-Mode Photothermal-Induced Resonance Spectroscopy. *Anal. Chem.* **2020**, *92*, 3544−3554.
(22) Li, S.; Zhang, Q. The Dielectric Properties of Low Temperature Thermally Cross-Linked Polystyrene and Poly(Methyl Methacrylate) Thin Films. *RSC Adv.* **2015**, *5*, 28980−28984.
(23) Hamm, P.; Lim, M.; Hochstrasser, R. M. Structure of the Amide I Band of Peptides Measured by Femtosecond Nonlinear-Infrared Spectroscopy. *J. Phys. Chem. B* **1998**, *102*, 6123−6138.
(24) Kim, Y. S.; Hochstrasser, R. M. Chemical Exchange 2D IR of Hydrogen-Bond Making and Breaking. *Proc. Natl. Acad. Sci. U.S.A.* **2005**, *102*, 11185.

https://doi.org/10.1021/acs.jpcc.1c01268
J. Phys. Chem. C 2021, 125, 8333−8338